Optical Camera-Based Multiplexed Photonic Sensor System With Ultralow Detection Limit for Biomedical Applications

Laura Pérez-Sánchez, Ana Sánchez-Ramírez, Jonas Leuermann, and Iñigo Molina-Fernández

***Abstract*—Photonic sensors based on Mach–Zehnder interferometric architectures with phase-coherent readout have demonstrated their potential for the integration into medical diagnostic devices. Their compact design, low cost, and ability to detect multiple biomarkers make them potentially applicable for the point-of-care. Achieving both high throughput and optimal sensor performance requires a miniaturized interrogation system with multiplexed readout capability that facilitates alignment and at the same time offers a high signal-to-noise ratio (SNR). In this work, the use of an optical camera (OC)-based system suited for multiplexed integrated photonic sensor detection is investigated. Its system level model is derived to determine the SNR and its associated limit of detection (LOD). This model allows achieving optimal sensing performance by tuning the photonic chip, the optical system, and the camera detection parameters. In agreement with model expectations, experimental results show that this system allows reaching for bulk detection limits of $\sim 10^{-7}$ refractive index units (RIUs) for a system comprising three sensors, representing a state-of-the-art achievement.**

***Index Terms*—Limit of detection (LOD), Mach–Zehnder interferometer (MZI), multiplexed sensor, optical camera (OC), signal-to-noise ratio (SNR).**

I. Introduction

PHOTONIC integrated sensors are promising candidates for medical diagnostics, in particular for simultaneous detection of multiple biomarkers [1], [2]. Over the last decade, there has been significant research on silicon-based biosensors. This growth is due to their potential for compact multiplexed operation, as well as cost-effectiveness, enabled by CMOS manufacturing compatibility. Additionally, interferometric sensing architectures, such as the Mach–Zehnder interferometer (MZI), have enabled highly sensitive real-time detection without the need for labels. These advantages provide a new opportunity for the economic large-scale production of single-use sensor chips for point-of-care (PoC) diagnostics [3].

To detect extremely low concentrations of biomarkers, the photonic chip and readout system must be carefully co-designed. This becomes clear when considering the photonic limit of detection (LOD), given by $\text{LOD} = 3\sigma/S$ [4]; the sensitivity (S) is contingent on the chip design, while the system noise (σ) directly depends on the readout system. To date, the lowest experimental LOD reported is of the order of 10^{-8} refractive index units (RIUs) [2], achieved with a coherently detected MZI-based silicon nitride sensor using a single sensor with a photodiode readout [5]. In that work, Leuermann et al.[5] analyzed the different noise sources and their fundamental impact on the LOD.

In multiplexed detection, image sensors have been widely used to capture multiple signals from the sensing chip surface due to several advantages [2], [6], [7]: 1) the typically high spatial resolution of the optical signals makes the alignment of silicon nitride sensors operating at telecom wavelengths (e.g., 1310 and 1550 nm) a much more straightforward procedure [6] and 2) optical camera (OC)-based systems provide enhanced stability during the alignment process compared to discrete readout systems. This advantage arises because mechanical micro-misalignments, which are known to be a source of degradation in discrete readout systems due to their association with mechanical noise and crosstalk issues [5], are more easily corrected in OC systems. This is supported by the ability to select integration regions via software, thereby excluding pixels that could potentially degrade system performance.

Cameras have been widely used for biosensing [8], [9], [10], [11] and more recently have been proposed as an alternative to photoreceivers in optical communication systems, a growing field that is commonly known as OC communications (OCCs) [12], [13]. There, the impact of the signal-to-noise ratio (SNR) on the system performance has been extensively characterized and modeled [14], [15] allowing a systematic optimization. Given the substantial influence of the camera parameters on the system performance [16], [17], applying this approach to the analysis and design of a multiplexed photonic sensing system incorporating an OC readout is imperative.

We propose the use of an OC as a readout detection system for multiplexed photonic sensors based on an MZI with

Received 7 July 2025; accepted 31 August 2025. Date of publication 22 September 2025; date of current version 1 October 2025. This work was supported in part by the Ministerio de Ciencia e Innovación y Universidades and the Agencia Estatal de Investigación, Spain, under Grant DIN2022-012816, Grant PRE2020-096438, and Grant TED2021-130400B-I00; in part by the Ministerio para la Transformacióon Digital y de la Función Pública, Spain (Plan de Recuperación, Transformación y Resiliencia, NextGenerationEU., MICROELECTRONICS), under Grant TSI-069100-2023-0013; and in part by the Universidad de Málaga, Spain. The Associate Editor coordinating the review process was Dr. Rajan Sarkar. *(Corresponding author: Laura Pérez-Sánchez.)*

Laura Pérez-Sánchez is with BIOHERENT S.L, 29590 Málaga, Spain, and also with the Photonics and RF Research Lab, Telecommunication Research Institute (TELMA), University of Malaga, 29010 Málaga, Spain (e-mail: lperez@bioherent.com).

Ana Sánchez-Ramírez and Iñigo Molina-Fernández are with the Photonics and RF Research Lab, Telecommunication Research Institute (TELMA), University of Malaga, 29010 Málaga, Spain, and also with IBIMA-BIONAND, Malaga Tech Park, 29590 Málaga, Spain.

Jonas Leuermann is with BIOHERENT S.L, 29590 Málaga, Spain.

Digital Object Identifier 10.1109/TIM.2025.3612559

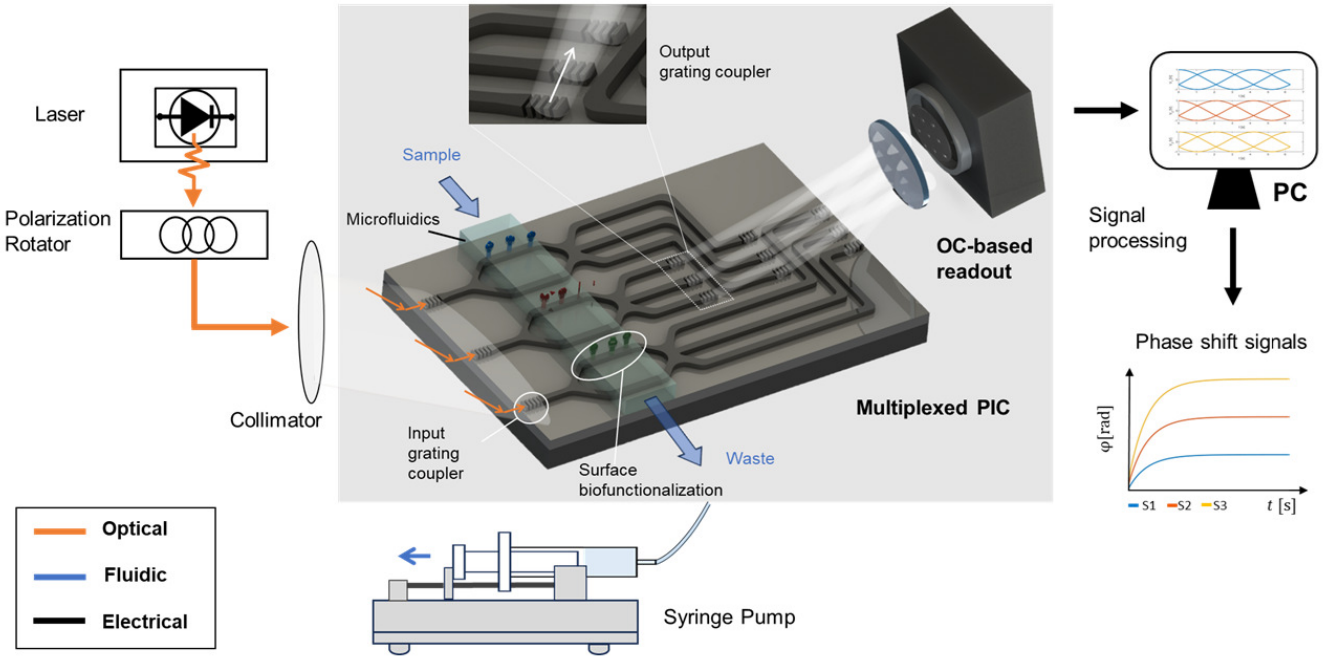

Fig. 1. Scheme of a multiplexed biosensor system-based on MZI with coherent phase detection and OC-based readout. The biosensor system comprises the light injection system (the laser source, the polarization rotator, and the collimator), the multiplexed integrated chip (PIC), the microfluidic system (a microfluidic chamber and a syringe pump), the OC-based readout (the lens and the camera), and the signal processing station consisting of a computer.

coherent phase detection. The system comprises a photonic chip, which contains three sensors, based on an MZI architecture with coherent readout [5]. The optical input/output of the chip is obtained by grating couplers (GCs), and the fluid under test is allowed to flow over the surface of the chip by means of a microfluidic cell. The novelty of this work lies in the reading system that consists of a lens and an OC. The lens maps and magnifies the near-field of the output GCs onto the camera sensor plane. Over the image of each GC, a region of interest (ROI) is chosen, which defines the pixels whose sum measures the optical power of each output GC. Fig. 1 illustrates the proposed sensing system and its potential for biomedical applications. As the bio-recognition process is not covered in this study, our focus is on the design and analysis of the photonic integrated chip (PIC) and the OC-based readout system. We are confident in its applicability as a biosensor, as PICs with the same design characteristics have been successfully used for the detection of biomolecules such as C-reactive protein (CRP) in [18].

To optimize the photonic LOD and SNR, a simplified systemic model of the OC-based system is proposed, allowing the evaluation of the LOD as a function of different design parameters, that is, laser power (P_0), optical magnification (M), ROI number of pixels (N_{ROI}), exposure time (T_{e}), sample rate (f_s), and electrical bandwidth (f_0). Proper selection of these parameters enables us to reach a state-of-the-art experimental photonic LOD of around 10^{-7} RIU, in good agreement with the model predictions.

The rest of the article is structured as follows. In Section II, we propose the MZI sensor setup and theoretically analyze the signal model and noise sources of an OC-based system for a multiplexed readout application. The analysis of the final SNR of the sensor is described in Section III. The equipment and the measurement procedure to validate the model are then described in Section IV. The influence of the camera parameters on the photonic LOD and the experimental result of the LOD after optimization are shown in Section V. Finally, the conclusions are drawn in Section VI.

II. Proposed Sensor Model

The proposed OC-read photonic sensor setup is shown in Fig. 2 (the actual system comprises three multiplexed sensors but only one is shown for the sake of clarity). The interferometric sensing system can be divided into three parts: 1) the light injection system; 2) the photonic integrated chip (PIC); and 3) the readout system.

A. Light Injection System and Photonic Integrated Chip

The incoming light is emitted by a laser source of wavelength λ_0 and power P_0, followed by a polarization rotator that adjusts the horizontal polarization for which the GC was designed [19]. With the aid of a collimator, a beam of light is incident on the input GC. The input light system is designed to ensure that the beam produces an output spot wide enough to fully cover the input GC area. After being coupled into the chip, the power is equally divided among the MZI sensors. Therefore, the input power for each sensor can be formulated as $P_{\mathrm{in}}(t) \propto P_0(t)/N_{\mathrm{BS}}$, N_{BS} being the number of sensors. Any substance flowing close over the sensing arm's surface can potentially cause a change in the effective refractive index of the guided modes, resulting in a phase shift $\varphi(t)$ between the sensing and reference signals. These two signals are connected to a 2×3 multimode interference coupler (MMI), whose

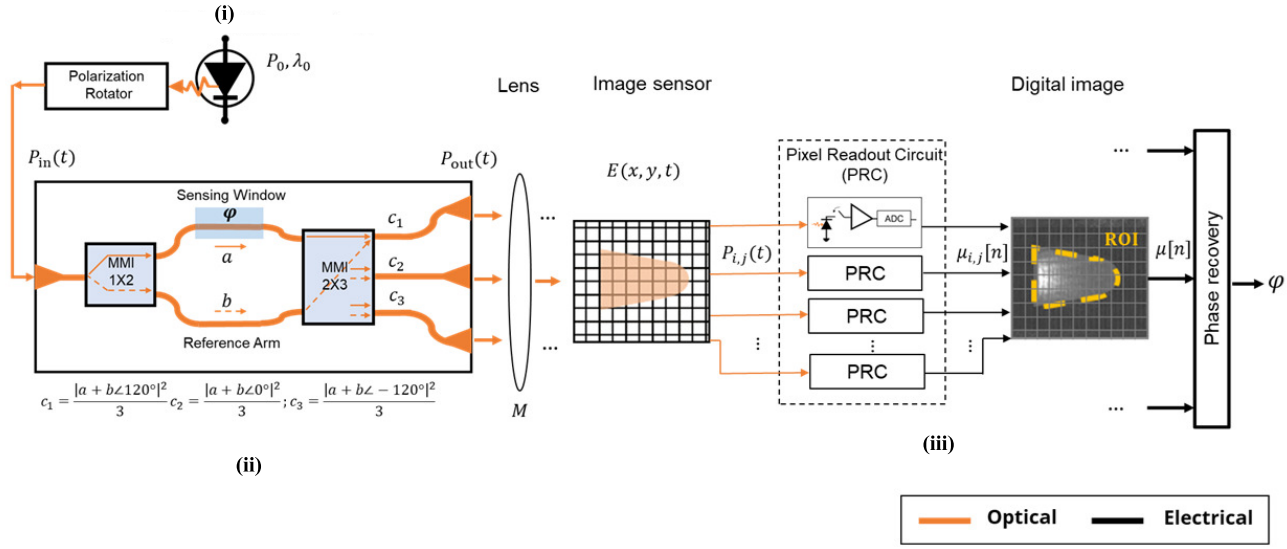

Fig. 2. Setup of the interferometric sensor with OC-based readout system: 1) light injection system is composed of a laser and a polarization rotator; 2) PIC is an MZI-based sensor with coherent phase detection; and 3) readout system is formed by a lens and a camera device, which capture the output optical power signals, $P_{out}(t)$, (detailed in Fig. 3). By applying imaging techniques and digital signal processing, the phase shift, φ, is recovered.

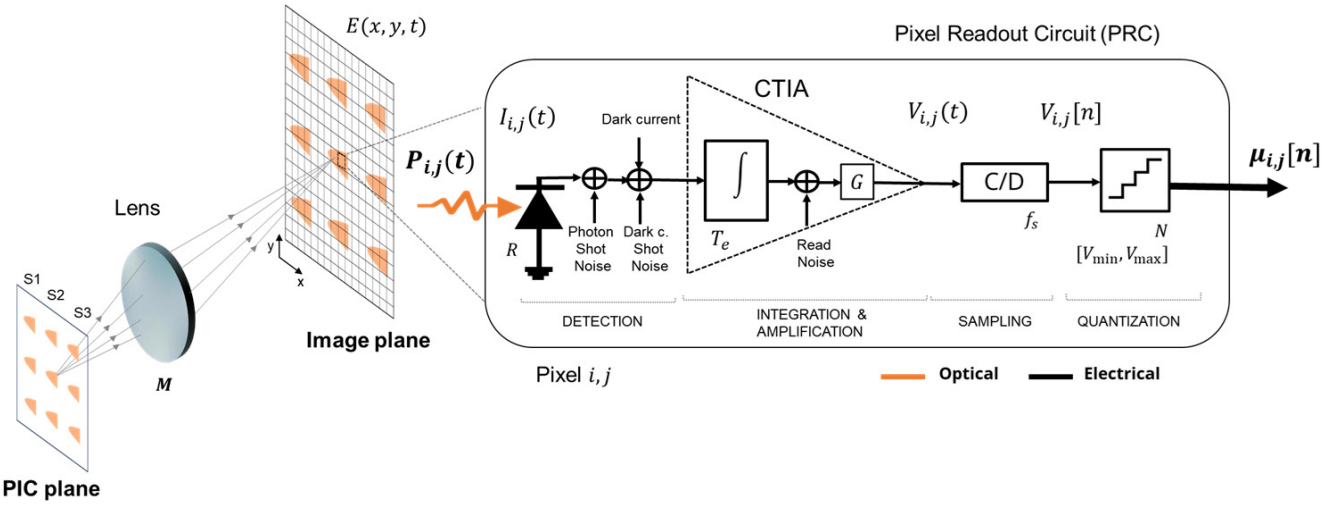

Fig. 3. Pixel readout model of the optical power in a single pixel, with electrical noise sources. The process of photo-detection, amplification, sampling, and quantification introduces sources of noise. These contributions include photon shot noise, dark current shot noise, and readout noise.

three outputs radiate toward the image sensor via GCs, as shown in Fig. 2. After detection and the necessary image processing, the three power signals $P_{out}(t)$ for each MMI's output can be easily calculated. As described in [20] and [21], the complex interferometric signal $S_c = A_c e^{j\varphi}$ can be derived from those three output signals, making an extraction of $\varphi(t)$ straightforward.

Here, it should be mentioned that P_{out} accounts for insertion losses (attributable to fiber connection losses, waveguide propagation losses, etc.), coupling losses (arising from the coupling of light in/out of the chip), and absorption losses (due to the substance flowing through the sensing window) [4].

B. OC-Based Readout System

1) Signal Model: The radiation (near field) of the output GCs is imaged, through an optical system, to the camera sensor plane (see Fig. 2). At this plane, the irradiance E of each GC can be formulated as follows:

$$E(x,y,t) = P_{out}(t)\, F(x,y) \tag{1}$$

where (x, y) are the coordinates of the image plane, and $F(x, y)$ governs how the GC output power $P_{out}(t)$ is distributed over the sensor plane. Due to the imaging system, this function is an M-fold magnified version of the output GCs near field. Each discrete pixel (i, j) captures only a fraction of the output power, which depends on its area A_{pixel} as follows:

$$P_{i,j}(t) \simeq E(x,y,t)\, A_{pixel} \tag{2}$$

where $i = x/(A_{pixel})^{1/2}$ and $j = y/(A_{pixel})^{1/2}$, assuming square pixels. Fig. 3 shows the readout model for each pixel. The

optical power captured by one pixel is converted into a photo-current as follows:

$$I_{i,j}(t) = RP_{i,j}(t) \tag{3}$$

where R represents the responsivity of the photo-active area.

Consecutively, for a set exposure time T_e, the photo-current is integrated and amplified by a capacitive transimpedance amplifier (CTIA) with a gain $G[\mathrm{V/e^-}]$ yielding an output voltage as follows:

$$V_{i,j}(t) = \frac{G}{q}\int_{T_e}^{T_e+t} I_{i,j}(\tau)\, d\tau \tag{4}$$

with q being the electron charge.

As shown in Fig. 3, the dark current signal for a temperature $\mathcal{T}$, denoted as $I_{d_{i,j}}(t,\mathcal{T})$, arises from thermally induced electrons [22]. Although its contribution can be minimized by image sensor calibration [23], it introduces shot noise ($\sigma^2_{d_{i,j}}$) that must be considered during the noise modeling.

Finally, the continuous voltage signal is digitalized using an ADC with a sampling frequency f_s, resulting in $V_{i,j}[n] = V_{i,j}(t)|_{t=n/f_s} = \mu_{i,j}\Delta_{\mathrm{ADC}}$, with $\Delta_{\mathrm{ADC}} = (V_{\max} - V_{\min})/2^N$ the quantization step and N the number of bits of the ADC. Note that $\mu_{i,j}$, from here on referred to as digital number (DN), is a natural number that satisfies $V_{\min} \le V_{\min} + \mu_{i,j}\Delta_{\mathrm{ADC}} \le V_{\max}$. This way, the n-th camera frame is represented as a matrix of digital numbers.

As represented in Fig. 2, the optical power received by each GC is calculated by summing the pixel values within its corresponding ROI. To ensure optimal performance, each ROI should be selected to maximize the SNR, as explained in Section II-B3.

The DN for each GC is given by the following:

$$\mu[n] = \sum_{i_{\mathrm{ROI}}}\sum_{j_{\mathrm{ROI}}} \mu_{i,j}[n] \tag{5}$$

where $(i_{\mathrm{ROI}}, j_{\mathrm{ROI}})$ are the pixel indices within the ROI assigned to each GC. Note that $\mu \propto P_{\mathrm{out}}$; therefore, by processing the three signals corresponding to each 2×3 MMI output, the sensor phase shift $\varphi(t)$ can be estimated.

2) Noise Sources: Several noise sources, each defined by its variance ($\sigma^2_{i,j}$), are considered in the pixel reading process, as illustrated in Fig. 3. Photon shot noise (e) and dark current shot noise (d) are generated during the photo-detection of the optical signal and the appearance of the dark current signal due to the thermally induced electrons [22], respectively. Read noise (r) accounts for the noise during the signal quantification process (electronics, quantization, etc.) [24]. All of them are modeled as white Gaussian noise processes so that the noise in each pixel depends on the total power spectral density ($\eta_{i,j}$) and the measurement bandwidth (B_w), $\sigma^2_{i,j} = \int_{B_w} \eta_{i,j}\, df$.

Regarding shot noise sources, the power spectral densities of the signal and dark current shot are given by the following:

$$\eta_{e_{i,j}} = 2qR\bar{P}_{i,j} \tag{6a}$$

$$\eta_{d_{i,j}} = 2q\bar{I}_{d_{i,j}} \tag{6b}$$

where $\bar{P}_{i,j}$ is the average received power at the pixel (i, j), and $\bar{I}_{d_{i,j}}$ is the average dark current. Assuming uncorrelated noise, the power spectral densities of the shot noises in an ROI are given by the following:

$$\eta_e = \sum_{i_{\mathrm{ROI}}}\sum_{j_{\mathrm{ROI}}} \eta_{e_{i,j}} \tag{7a}$$

$$\eta_d = \sum_{i_{\mathrm{ROI}}}\sum_{j_{\mathrm{ROI}}} \eta_{d_{i,j}}. \tag{7b}$$

Read noise constitutes a significant noise source in OC systems. Typically, manufacturers characterize the read noise during device calibration and express it in units of electrons, referenced to the integrator output. Consequently, the variance of the read noise associated with each output is given by the following:

$$\sigma^2_r = \sum_{i_{\mathrm{ROI}}}\sum_{j_{\mathrm{ROI}}} \sigma^2_{r_{i,j}}. \tag{8}$$

While the quantization noise is easy to deduce from the quantification step, $\sigma^2_q = \Delta^2_{\mathrm{ADC}}/12$, rest of the noise sources cannot be estimated theoretically because the values and parameters required to calculate them are not included in the camera datasheet.

The proposed noise model is limited to characterizing noise sources of electrical origin, specifically those arising from the readout system. As is well known in the field of photonic sensing, mechanical noise due to micro-misalignment and signal fluctuations caused by temperature variations can significantly impact the low detection limits that characterize these systems. However, the careful design of peripheral systems surrounding the photonic chip, such as microfluidics, temperature controller, and the light injection system, among others, has allowed us to disregard other drift sources and focus the modeling exclusively on electrical noise sources.

3) ROI Shape and Optimization: A crucial step in optimizing sensor readout using an OC-based system is the selection of the ROI. We propose creating a binary mask based on the shape of the near field profile of the sensor's output GC, which will be applied to all frames during the processing. The mask enables us to exclude pixels that could degrade the final SNR of each output and, consequently, the LOD of the system.

The designed GC features an exponentially decaying field along the propagation axis (y) and a Gaussian distribution in the orthogonal direction (x) [25], [26]. Accordingly, given that $y = 0$ represents the origin point for the radiance of the GC, the irradiance distribution in the image sensor plane for $y \ge 0$ can be defined as follows:

$$E(x,y) = E_0 e^{-2\frac{x^2}{w_0^2}} e^{-\alpha y} \tag{9}$$

where w_0 is the modal field radius of the Gaussian, α is the radiation decay factor, and E_0 is the maximum irradiance value (at point $x = y = 0$).

The ROI selection criterion is based on including only those pixels whose signals levels positively contribute to the overall SNR, that is, where the signal significantly exceeds the noise. Including pixels with low irradiance increases the total noise contribution, particularly from read noise, without providing substantial signal information, thus degrading the SNR. Therefore, given the predominance of read noise in

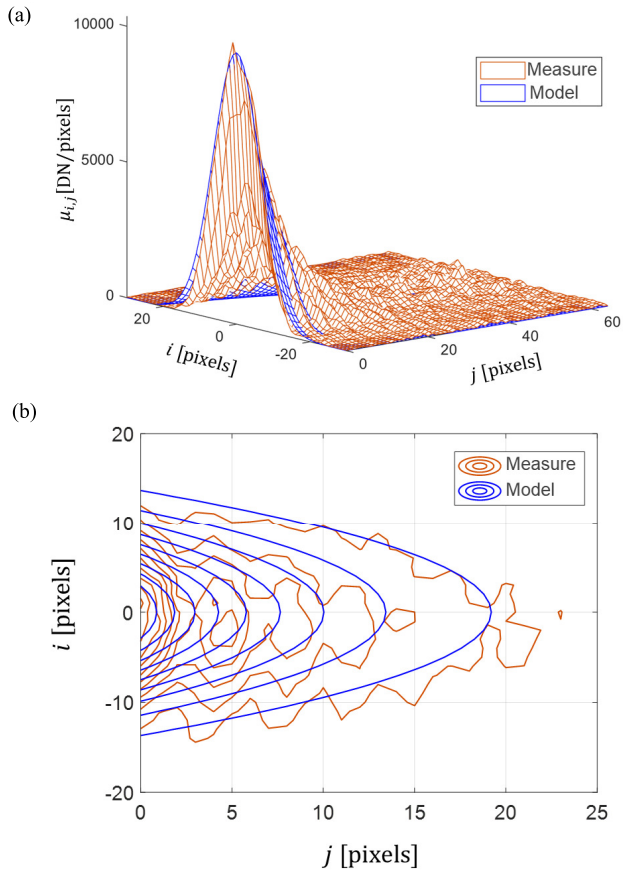

Fig. 4. Comparison of the sensor output irradiance model and experimental measurements: (a) mesh plot and (b) contour plot.

regions of low irradiance and assuming spatially uniform noise characteristics, the ROI shape is determined by constant irradiance curves. This approach ensures that the pixel summation optimally balances signal contribution and noise addition. These contours are modeled as parabolic profiles defined by the following:

$$F(x, y) = g(E) \tag{10}$$

where E is a constant. Assuming that $E(x, y)$ remains constant over time, (9) allows modeling the spatial power distribution of the GC near field at any given instant.

Fig. 4(a) compares the irradiance model with experimental data, showing excellent agreement with parameter optimization, with errors below 8%. Fig. 4(b) presents a contour plot overlaying the irradiance model and measured results, clearly illustrating the ROI shape defined by constant irradiance curves.

III. Analysis of the SNR

In a coherent MZI sensor, the readout system performance typically is evaluated in terms of SNR due to its impact on the LOD. We first determine the overall SNR of the sensor by analyzing the frequency response of the signal and the noise, and then establish its relationship to the LOD. Finally, the influence of the camera-captured parameters on the SNR is evaluated for LOD optimization.

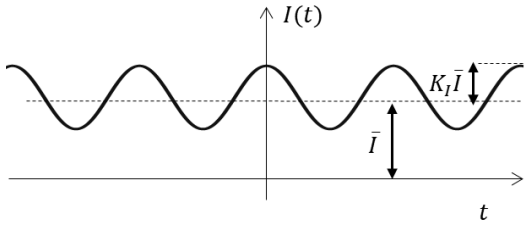

Fig. 5. Photo-current signal of a single output showing fringe contrast $1/K_I$ of the interferogram due to MZI unbalance.

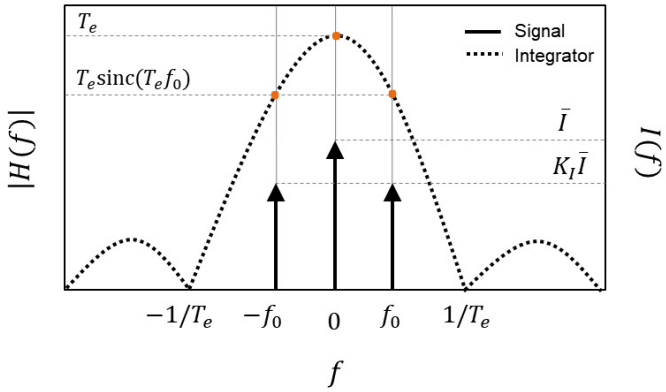

Fig. 6. Spectrum of the signal and frequency response of the integrator. The solid line represents the spectrum of the signal, while the dotted line depicts the magnitude of $H(f)$.

A. SNR Model

To simplify the model, we assume that the phase of the signal in the sensing arm increases linearly over time, resulting in a sinusoidal interferogram. Consequently, the photo-current of each output can be written as follows:

$$I(t) = \bar{I} + K_I \bar{I} \sin(2\pi f_0 t) \tag{11}$$

where $1/K_I$ is the fringe contrast of the interferogram due to the unbalance of the MZI (see Fig. 5) and f_0 is the frequency of the signal. Here, we use K_I to denote the ratio of the direct component of the photo-current at each output ($\bar{I} = R\bar{P}_{\text{out}}$) and its alternating component. Only the latter is of interest, as it is the signal carrying most of the information, thus, mainly contributing to the SNR. According to [4], K_I is a function of the absorption losses and the length of the sensing arm L_s.

After the detection, the signal passes through an integration circuit with a frequency response of $H(f) = e^{-j\pi T_e/2} T_e \text{sinc}(T_e f)$. Fig. 6 illustrates the magnitude of the frequency response for both the photo-current signal and the integrator. Finally, the signal is amplified and digitized.

Presuming a sampling frequency above the Nyquist rate and considering only the $K_I \bar{I} \sin(2\pi f_0 t)$ term, the digital output information signal is given by the following:

$$\mu = \frac{1}{\sqrt{2}} \frac{K}{q} K_I \bar{I} T_e \text{sinc}(T_e f_0) \tag{12}$$

where $K = G/\Delta_{\text{ADC}}$ is the overall conversion gain of the image sensor.

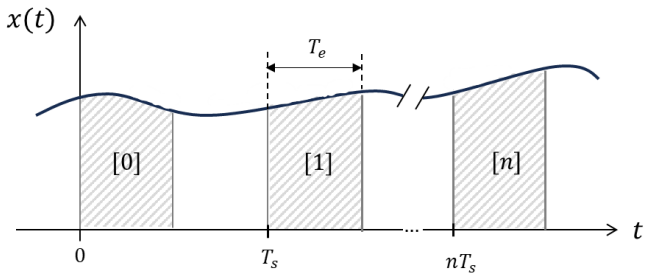

Fig. 7. Integration and sampling steps of an arbitrary signal, $x(t)$, where $T_s = n/f_s$.

Shot noise—originating from the photo-current and dark current—is also integrated, amplified, and digitized, as shown in Fig. 7. Assuming a Gaussian white noise process with a power spectral density $\eta_e + \eta_d$ at the integrator input, the total noise variance over a bandwidth $B_w = f_0$ becomes as follows:

$$\sigma^2 = C\frac{K^2}{q^2}\frac{2f_0}{f_s}\left(\eta_e T_e + \eta_d T_e + \sigma_r^2 q^2\right) \tag{13}$$

where C represents the noise correlation factor, which depends on the average correlation coefficient between neighboring pixels (ρ) and the total number of pixels (N_{ROI}). It is defined as follows:

$$C = 1 + (N_{\text{ROI}} - 1)\rho. \tag{14}$$

Pixel noise correlation in camera sensors, due to capacitive coupling, is well known in the literature [27]. Not accounting for this effect results in an underestimation of the actual noise level, even though the noise correlation between neighboring pixels is typically very low (less than 3%–6% as reported in [28]).

From (12) and (13), we calculate the SNR for a single ROI at the output of the OC-based readout system as μ^2/σ^2 as follows:

$$\text{SNR}_{\text{ROI}} = \frac{K_I^2 R^2 f_s}{4\,C}\frac{P_{\text{out}}^2 T_e}{f_0\left(\eta_e + \eta_d + \frac{\sigma_r^2 q^2}{T_e}\right)}\text{sinc}^2\left(T_e f_0\right). \tag{15}$$

The output SNR of the readout system is significantly affected by short integration times and high pixel noise correlation. Finally, the LOD can be written as follows:

$$\text{LOD} = \frac{3}{\sqrt{2}}\frac{\sigma}{S} = \frac{3\lambda_0}{S_{\text{wg}}\pi}\frac{1}{L_s\sqrt{\text{SNR}}} \tag{16}$$

where $S = (2\pi/\lambda_0)S_{\text{wg}}L_s A_c$, with S_{wg} the waveguide sensitivity and A_c the amplitude of the complex interferometric signal, and $\text{SNR} = 3\,\text{SNR}_{\text{ROI}}$; the overall SNR of the sensing system, given that three outputs per sensor are used for the coherent reading [4].

B. Impact of Camera Parameters on the SNR

According to (15) and (16) optimizing the OC-based readout system requires careful selection of camera parameters to enhance the performance of photonic biosensors.

We consider a sensing system with N_{BS} multiplexed sensors and N_{out} GCs per sensor for coherent readout. Furthermore, the total number of pixels in the image sensor with full well capacity (FWC) is N_{IS}. The FWC is defined as the number of electrons that a pixel can collect at saturation level [22].

In addition, for the sake of simplicity, and to obtain simple design rules, we assume the following:

1) GCs are placed without space between them, and M is chosen so the entire GC array fits within the image sensor area. Under these conditions, the maximum pixels per ROI is given by the following:
$$N_{\text{ROI}} = \frac{N_{\text{IS}}}{N_{\text{out}}N_{\text{BS}}}. \tag{17}$$
2) The irradiance distribution of each GC is uniform, that is, the power in each pixel belonging to the ROI is $P_{i,j} = P_{\text{out}}/N_{\text{ROI}}$.

Equations (15) and (16) show that maximizing the product $P_{\text{out}}^2 T_e$ is essential to optimize the LOD. Since FWC constrains the $P_{i,j}T_e$ product, optimal performance is achieved when selecting the camera settings for full exposure operation, that is, $\text{FWC} = (P_{i,j}T_e)_{\max}$.

As the overall noise power results from the combination of the individual noise contributions, the LOD can be expressed as follows:

$$\text{LOD} \propto \sqrt{\text{SNR}_e^{-1} + \text{SNR}_d^{-1} + \text{SNR}_r^{-1}}. \tag{18}$$

To help design an OC system, we write out the individual factors associated with each SNR contribution [see (18)], including only the modifiable terms in the readout system as follows:

$$\text{SNR}_e \propto \frac{f_s}{C}N_{\text{ROI}}\text{FWC}\,\text{sinc}^2\left(T_e f_0\right) \tag{19}$$

$$\text{SNR}_d \propto \frac{f_s}{C}\frac{N_{\text{ROI}}}{I_{d_{i,j}}T_e}\text{FWC}^2\,\text{sinc}^2\left(T_e f_0\right) \tag{20}$$

$$\text{SNR}_r \propto \frac{f_s}{C}\frac{N_{\text{ROI}}}{\sigma_{r_{i,j}}^2}\text{FWC}^2\,\text{sinc}^2\left(T_e f_0\right). \tag{21}$$

Equations (19)–(21) indicate that increasing f_s, N_{ROI}, and FWC leads to an improvement in the SNR across all cases, whereas an increase in C negatively impacts the SNR. The noise correlation factor scales with N_{ROI}, and it is typically absent from datasheets. It is advisable to contact the manufacturer or characterize this factor before selecting a suitable camera.

To operate under full exposure conditions, the $P_{i,j}T_e$ product must be tuned to the pixel FWC. Minimizing T_e is beneficial because of the following.

1) The maximum sampling frequency $f_{s,\max} = (T_e + T_r)^{-1}$ depends on both the fixed readout time T_r (for cameras typically in the order of milliseconds), and the configurable T_e.
2) The dark current shot noise can be considered negligible as photon shot noise and read noise dominate at low exposure levels.
3) If $f_0 \ll T_e^{-1}$, the signal attenuation term $\text{sinc}^2(T_e f_0)$ can be neglected.

Thus, reducing T_e while tuning P_{out} for full exposure maximizes performance. Furthermore, (20) and (21) show

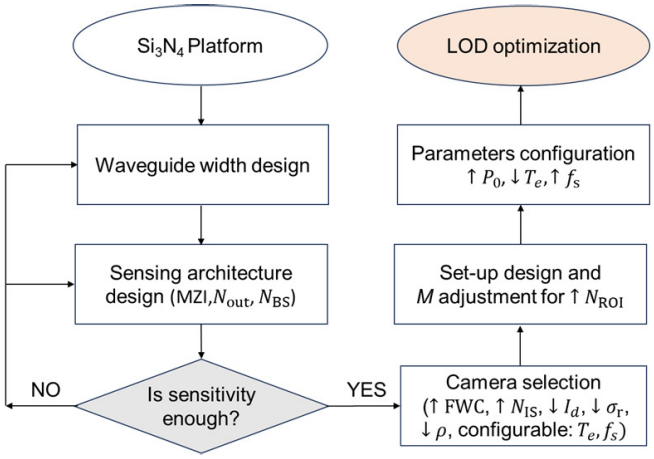

Fig. 8. LOD optimization steps.

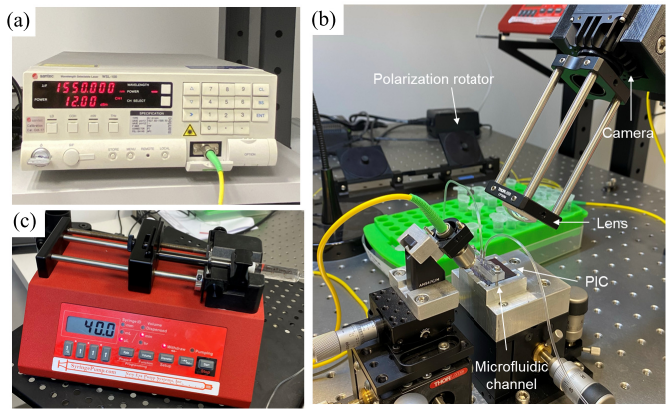

Fig. 9. (a) Used laser source and (b) applied syringe pump for fluid control. (c) Rest of the experimental setup showing the fiber polarization rotator, the PIC, the fluidic PDMS-based channel, and the OC-based readout system (lens + camera).

TABLE I
WIDY SENS 640V-ST CAPTURE PARAMETERS

Parameter	Value
Resolution	512x640 pixels
Pixel area, A_{pixel}	225 µm^2
Frame rate, f_s	up to 230 Hz
Exposure time, T_e	10 µs to 1 s
Quantum efficiency, QE	>70%
Quantization bits, N	14 bits
Dark current, $I_{d_{i,j}}$	50 ke$^-$/s
Full Well capacity, FWC	> 380 ke$^-$ (Low Gain)
	> 17 ke$^-$ (High Gain)
Read noise, $\sigma^2_{r_{i,j}}$	270 e$^-$ (Low Gain)
	50 e$^-$ (High Gain)

that $\text{SNR}_d \propto 1/I_{d_{i,j}}$ and $\text{SNR}_r \propto 1/\sigma^2_{r_{i,j}}$, emphasizing the importance of selecting a camera with minimal dark current and read noise. Fig. 8 outlines the steps to optimize LOD in an OC-based multiplexed sensing system.

IV. Experimental Methods

A. Measurement Setup

To validate the model, we use the sensor setup shown in Fig. 9. The equipment consists of a Santec WSL-100 laser source, a fluidic syringe pump (NE-1000 from New Era Pump Systems, Inc.), a sensing chip, and a readout system, based on an achromatic doublet (AC254-030-C from Thorlabs) and a WiDy-SenS 640V-ST SWIR (short-wave infrared) camera from NIT. Relevant key parameters of the camera are shown in Table I. We also use a temperature controller (TEC), composed of various components from Thorlabs (thermistor—TH10L, single-stage TEC element—TECF1S, TEC board—MTVDEVAL1, and TEC driver—MTD1020T), to maintain a stable temperature throughout the experiments.

In this setup, the laser emits the light signal at a wavelength of 1550 nm, which is the design wavelength of the sensors. The optical signal is then coupled into the chip using an input system consisting of lenses and a collimator. This system was designed to generate a beam diameter three times larger than the mode field diameter of the input GC. This configuration enhances angular and positional tolerance, at the expense of reduced coupling efficiency due to the mismatch between the incident beam size and the GC mode [26]. Nevertheless, it significantly mitigates mechanical noise caused by micro-misalignments, which is a common issue in injection systems based on optical fibers [5]. The multiplexed chip integrates three optically balanced MZI sensors ($N_{BS} = 3$) with $L_s = 7$ mm and $S_{wg} \sim 0.23$ RIU/RIU. The chip's layer stack consists of a silicon substrate, a 3-μm buried oxide (BOX) layer, and a 300-nm silicon nitride film, fabricated at Cornerstone, University of Southampton, Optoelectronics Research Center. A PDMS flowcell is used to form a fluidic channel for aqueous buffer solutions on top of the sensing arm.

The OC-based readout system, consisting of a lens and a camera, is responsible for capturing the signals from the output GCs. This process occurs in free space, making the design of the GCs crucial to ensure that the outgoing beams have the proper directivity and divergence to be initially captured by the lens and subsequently by the image sensor [29]. The positioning of the output GCs within the chip is a strategic step to fully optimize the use of the image sensor as well as the adjustment of M, playing a pivotal role in this process.

B. Data Processing

Once a raw data image is generated by the OC, it is attached to an array of frames. Fig. 10 illustrates the data processing workflow. First, non-uniformity corrections are applied to each frame to mitigate variations in pixel sensitivities and compensate for dark current influences onto the signals [22]. To maximize the SNRs, the raw images are multiplied by a binary mask, as shown in Fig. 10(b), which removes pixels that might degrade the final SNRs (see Section II-B3).

Subsequently, for each frame and ROI, the pixel DN values are summed, resulting in three signals per sensor as portrayed in Fig. 10(d). These are used to reconstruct the corresponding MZI complex signal I_c [21], from which its phase $\angle I_c = \varphi$ can be easily extracted [see Fig. 10(e)]. This entire process is performed with MATLAB.

V. Results

This section treats the experimental validation of the proposed readout model for a multiplexed photonic sensor using an OC-based system. We focus on previously identified factors

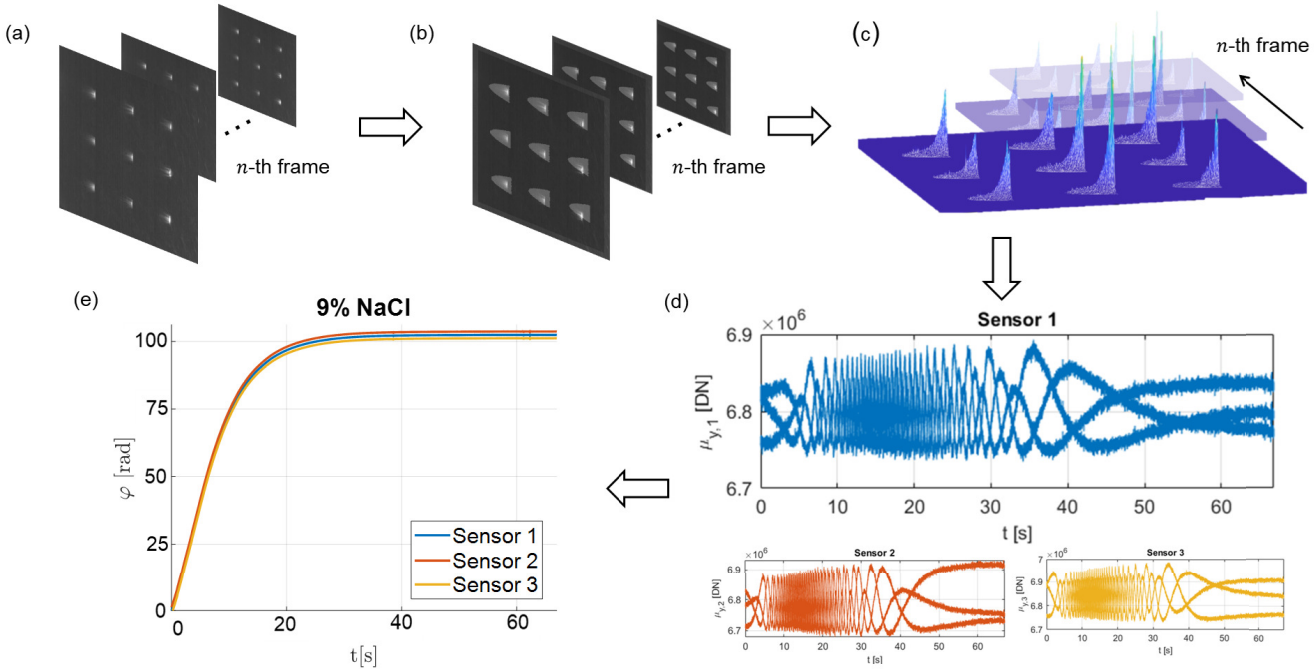

Fig. 10. Outline of the signal processing steps of a multiplexed sensor. (a) Raw data frames capturing the output optical power signals from the sensors. (b) Frames resulting from the processing (i.e., non-uniformity correction) and the application of the binary mask to define the ROI, and (c) 3-D representation of the power distribution in each ROI after removal of undesired pixels. (d) Integrated pixel values for each ROI, and (e) corresponding phase shifts after introducing a 9% sodium chloride (NaCl) solution.

that have the greatest impact on the optimization process (see Section III), examining each one separately.

First, we focus on pixel noise, confirming that the noise levels provided by the camera manufacturer align with our experimental measurements and the model's predictions. Furthermore, we investigate potential noise correlations between neighboring pixels, which might negatively impact the SNRs.

Finally, we apply the optimization strategies discussed earlier to experimentally demonstrate the achievable LOD under realistic operating conditions.

A. Noise Assessment

1) Pixel Noise: In the following, the noise analysis of a single pixel is discussed. The objective is to identify the dominant noise sources across varying exposure levels. We varied the optical input power across the full dynamic range (up to the FWC), repeating the measurement for different exposure times and pixels to confirm consistency with the manufacturer specifications. Fig. 11 shows the standard deviation curve (continuous black) and the sum of the theoretical noise (black and orange dashed) as a function of the electrons captured by a sensor pixel ($i = 290$ and $j = 418$) at $T_e = 10\ \mu$s. Experimental data (blue dots) are compared with the theoretical noise levels, confirming that read noise dominates at low signal levels, while shot noise prevails at higher exposures.

Short exposure times are of particular interest due to their critical influence on overall system SNR. In this case, the dark current's average was measured to be 56.6 ke$^-$/s which is 13.2% higher than specified in the OC datasheet. The average read noise, with a value of 330 e$^-$, was 14.1% above the

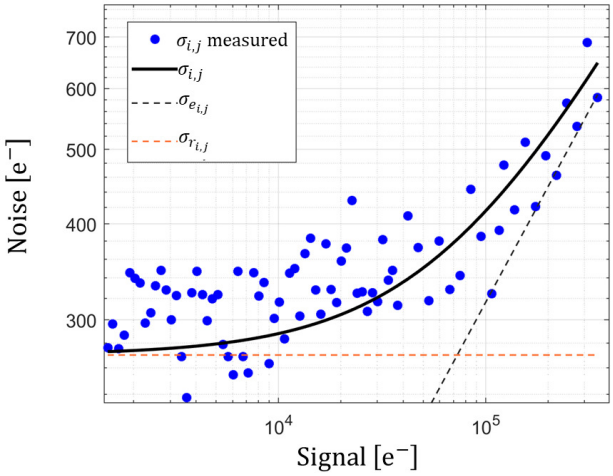

Fig. 11. Noise standard deviation as a function of the number of captured electrons. The manufacturer read noise (orange dashed), the theoretical photon shot noise (black dashed), the theoretical total noise (black line), and the measured total noise (blue dots) are shown.

manufacturer's specifications. Both measurements indicate the accuracy of our pixel noise model.

Considering the irradiance distribution (see Section II-B3), the central pixels within each ROI (at $y = 0$) capture the highest power, close to FWC and are thus dominated by shot noise. However, the remaining ROI pixels are dominated by read noise. Note that the dark current shot noise can be omitted due to the microsecond exposure times.

2) Correlated Noise: To evaluate the presence of correlated noise among neighboring pixels, we conducted an experiment analyzing the sensor's output noise.

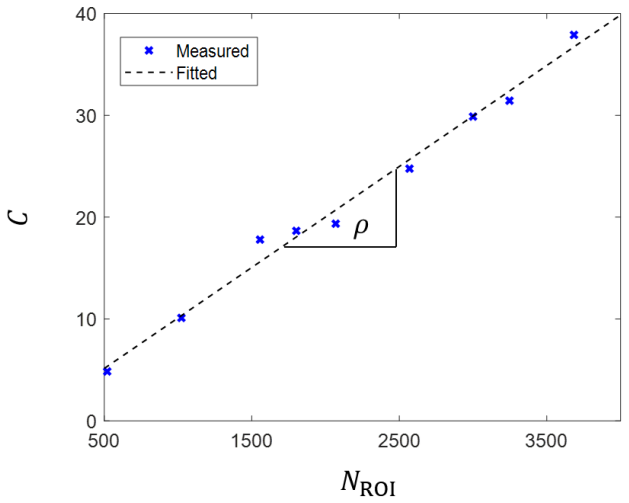

Fig. 12. Noise correlation between neighboring pixels in the WiDy-SenS 640V-ST camera.

TABLE II
MODEL SYSTEM KEY PARAMETERS

Parameter	Value	Parameter	Value
N_{out}	3	f_s	224 Hz
N_{ROI}	$\sim$ 3000 pixel	B_w	2 Hz
P_{out}	4 µW	M	3
K_I	0.69	K	23 DN/ke$^-$
T_e	10 µs	C	$\sim$ 30

The noise is computed as the variance of the output signal (Var(μ)) after aggregating all pixels within the ROI. If the noise was uncorrelated, Var(μ) should be equal to the sum of the individual noise contributions from each pixel, as described in (7a) and (8).

However, the experimental measurements show that the noise is linearly correlated with N_{ROI} (see Fig. 12) compared to the uncorrelated case, that is, $\text{Var}(\mu) = C(N_{ROI}) \sum_{i_{ROI}} \sum_{j_{ROI}} \sigma^2_{i,j}$, where $C(N_{ROI})$ is a linear function. From the slope of the curve, the correlation coefficient (ρ) is determined, confirming that, in this case, there is a 1% correlation between neighboring pixels. This demonstrates that correlated noise should not be disregarded, especially when N_{ROI} is large.

B. Sensitivity and LOD Measurement

According to the specifications outlined in Section III-B and the cameras acquisition parameters (Table I), the configurable parameters of the readout system were meticulously chosen to achieve the optimal LOD. The exposure time was chosen to be as short as possible, allowing us to operate at the maximum sampling rate. Moreover, maximizing the input power is essential to optimize the SNR since $P_0 \propto P_{out}$. However, the FWC, the camera resolution, and the number of multiplexed coherent MZI biosensors impose limitations on the selection of P_0.

Considering the given constraints, the distribution, and the shape of the output GCs on the chip, the adjustment of M allows us to optimize for the light incidence area on the image sensor, that is, adjusting N_{ROI} to maximize P_0.

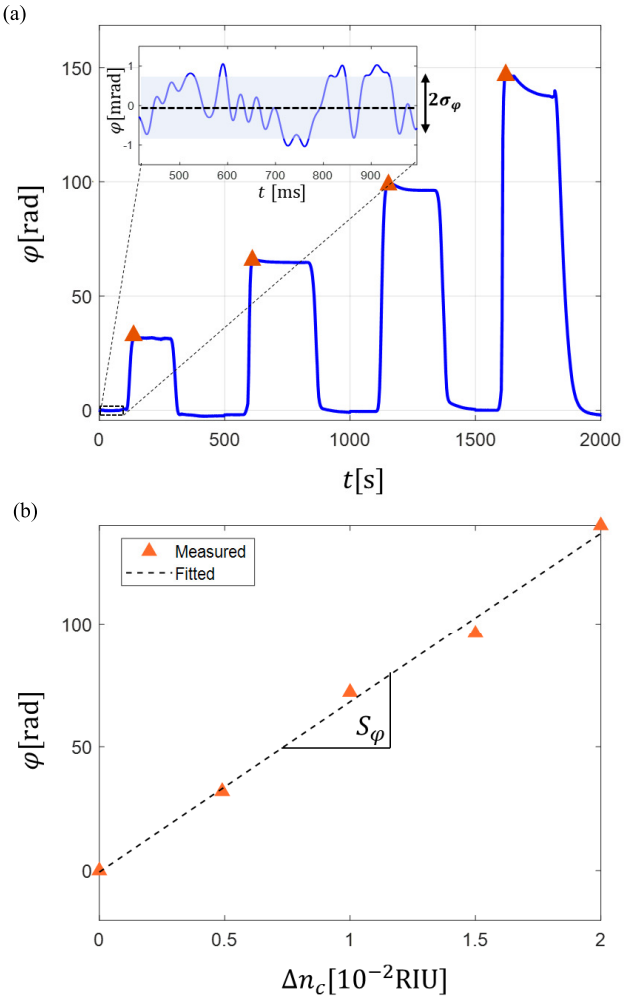

Fig. 13. (a) Example of a bulk sensing experiment for the extraction of phase noise and sensitivity. The inset shows the signal filtered to reduce high-frequency noise. (b) Phase variation curve versus refractive index variation in the cover to compute the overall sensitivity.

Table II presents the complete list of the setup parameters used, resulting in a theoretical LOD of 1.2×10^{-7} RIU.

A typical calibration procedure was employed to determine the experimental bulk LOD [5], involving the injection of de-ionized water (Milli-Q) solutions with varying concentrations of sodium chloride (NaCl) at a flow rate of 40 μL/min. The flow rate was carefully chosen to prevent the potential drift caused by microfluidic phenomena, such as bubble formation [30]. Additionally, the experiment is conducted at a controlled temperature of 25 °C using the TEC, ensuring greater system stability and minimizing drift-inducing factors. In (16), the LOD was defined in terms of the SNR; however, the LOD of a sensing experiment is obtained from the phase signal, due to $\text{LOD} = 3\sigma_\varphi / S_\varphi$, where σ_φ is the standard deviation of the phase signal [see inset of Fig. 13(a)] and S_φ the phase sensitivity [see Fig. 13(b)]. The equation is derived from the previously discussed parameters with $\sigma_\varphi = (N_{out})^{1/2}\sigma/(\sqrt{2}A_c)$, where $A_c = N_{out} K_I \bar{I}$ and $S_\varphi = (2\pi)/(\lambda_0) L_s S_{wg}$ [5].

The sensor response is linear, and the sensitivity is independent of the concentration of the solution used for calibration. As illustrated in Fig. 13(a), the phase changes over time for

TABLE III
COMPARISON OF BULK LOD VALUES OF INTERFEROMETRIC BIOSENSORS

Reference	Type	Detection capability	Readout system	LOD [RIU]
[32]	BiMW	Single	Photodetector	$5{\cdot}10^{-5}$
				$8.77{\cdot}10^{-6}$
[33]	BiMW	Single	Photodetector	2 - $5{\cdot}10^{-7}$
[5]	MZI	Single	Photodetector	$1.4{\cdot}10^{-8}$
[1]	MZI	Multiplexed	Camera	$2.24{\cdot}10^{-4}$
[34]	MZI	Multiplexed	Camera	$\sim 10^{-6}$
This work	MZI	Multiplexed	Camera	$3.4{\cdot}10^{-7}$

different flow injections of Milli-Q and four solutions with concentrations of 3%, 6%, 9%, and 12% NaCl, respectively. The orange triangle represents the settled phase changes that occur at these concentrations. According to [31], the refractive index (n_c) for each concentration is calculated, and the corresponding refractive index variation (Δn_c) relative to the buffer (in this case, Milli-Q) is determined for the different solutions. Finally, the phase sensitivity is defined as the slope of the curve of φ in relation to corresponding Δn_c [see Fig. 13(b)]. In this work, we obtained an overall sensitivity of 6867 rad/RIU. Phase shift noise was quantified at 0.8 mrad using time frames acquired with Milli-Q water over the sensor, following the application of a low-pass filter to attenuate high-frequency components [see Fig. 13(a)]. Subsequently, a detection limit of 3.4×10^{-7} RIU was determined, which is in excellent agreement with the theoretical number calculated from the SNR analysis done in this work. The slight discrepancies observed arise because the theoretical model uses average parameters provided by the manufacturer, which involve assuming ideal conditions for certain parameters. In particular, the model assumes linearity and does not account for sensor non-uniformities such as pixel-to-pixel variations in dark current or read noise, which can affect the behavior of the actual system and experimental results.

Table III presents a detailed comparison of various interferometric biosensor configurations. For reference, both MZI and bimodal waveguide (BiMW) biosensors are included. The table highlights their detection capabilities, distinguishing between single and multiplexed detection, as well as their respective bulk LOD values.

VI. CONCLUSION

Camera capture parameters significantly impact the LOD of multiplexed coherent MZI sensors. Our derived model clearly indicates that low exposure times and high sampling frequencies maximize the system's SNR. Furthermore, non-configurable parameters such as the FWC and image sensor resolution not only affect SNR optimization but also limit the readout multiplexing capability in ultralow LOD sensor design.

Our results also show the SNR at the signal-level output is further degraded by pixel-level integration processes and correlated noise among neighboring pixels. We experimentally achieved an exceptional LOD of 3.4×10^{-7} RIU through the optimal selection of camera parameters, a carefully designed MZI sensor configuration, and ROI optimization strategies. This result aligns well with our theoretical model and demonstrates state-of-the-art photonic sensing capabilities.

This work introduces a theoretical model that effectively describes the behavior of camera-based readout systems for photonic biosensors. In contrast to previous models that assume ideal image sensors, our approach accounts for real-world effects such as pixel non-uniformities and inter-pixel correlated noise. However, the model does not consider certain limitations, including performance degradation over time due to sensor aging or environmental factors. These aspects were not explored in this study, as all experiments were performed under controlled conditions with active temperature regulation and mechanical isolation. Future work should address these factors, particularly for long-term or field-deployable biosensing applications.

Thus, we can confidently assert that OC-based readout systems are an excellent alternative to classical photodetector-based systems due to their numerous advantages.

1) Enhanced miniaturization in highly multiplexed sensing systems.
2) High adaptability of the readout system to different photonic chip layouts, enabled by the lens-based optical system and the ability to select the position and shape of the ROI for each output.
3) Mitigation of micro-misalignment issues through software-based ROI position corrections.
4) Simplified alignment process. Discrete photodiode-based systems typically require prior coupling of the optical signal to a fiber or fiber array before connecting to the photo-detector. In contrast, OC-based systems perform signal readout in free space, eliminating this additional step.

This reinforces the suitability of OC-based detection for highly multiplexed photonic sensing applications, offering increased flexibility, robustness, and ease of integration. Moreover, we are confident in the scalability of our approach to other biosensor architectures, as well as to other research fields that utilize cameras and require SNR optimization to enhance their performance.

REFERENCES

[1] D. Kohler et al., "Biophotonic sensors with integrated Si_3N_4-organic hybrid (SiNOH) lasers for point-of-care diagnostics," *Light, Sci. Appl.*, vol. 10, no. 1, p. 64, Mar. 2021.

[2] J. C. Ramirez, D. Grajales García, J. Maldonado, and A. Fernández-Gavela, "Current trends in photonic biosensors: Advances towards multiplexed integration," *Chemosensors*, vol. 10, no. 10, p. 398, Sep. 2022.

[3] M. Estévez, M. Álvarez, and L. M. Lechuga, "Integrated optical devices for lab-on-a-chip biosensing applications," *Laser Photon. Rev.*, vol. 6, no. 4, pp. 463–487, 2011.

[4] Ì. Molina-Fernández, J. Leuermann, A. Ortega-Moñux, J. G. Wangüemert-Pérez, and R. Halir, "Fundamental limit of detection of photonic biosensors with coherent phase read-out," *Opt. Exp.*, vol. 27, no. 9, pp. 12616–12629, 2019.

[5] J. Leuermann et al., "Optimizing the limit of detection of waveguide-based interferometric biosensor devices," *Sensors*, vol. 19, no. 17, p. 3671, Aug. 2019.

[6] L. Torrijos-Morán, B. D. Lisboa, M. Soler, L. M. Lechuga, and J. García-Rupérez, "Integrated optical bimodal waveguide biosensors: Principles and applications," *Results Opt.*, vol. 9, Dec. 2022, Art. no. 100285.

[7] A. Densmore et al., "Silicon photonic wire biosensor array for multiplexed real-time and label-free molecular detection," *Opt. Lett.*, vol. 34, no. 23, pp. 3598–3600, 2009.

[8] S. Rampazzi, G. Danese, F. Leporati, and F. Marabelli, "A localized surface plasmon resonance-based portable instrument for quick on-site biomolecular detection," *IEEE Trans. Instrum. Meas.*, vol. 65, no. 2, pp. 317–327, Feb. 2016.

[9] A. K. L. Freitas and L. C. Oliveira, "A portable surface plasmons resonance sensor based on single-board computer," *IEEE Trans. Instrum. Meas.*, vol. 72, 2023, Art. no. 9501509.

[10] N. J. Goddard, H. J. Dixon, N. Toole, and R. Gupta, "3-D printed instrumentation for point-of-use leaky waveguide biochemical sensor," *IEEE Trans. Instrum. Meas.*, vol. 69, no. 9, pp. 6390–6398, Sep. 2020.

[11] C. A. D. S. Filho, A. M. N. Lima, and H. Neff, "Smartphone based, portable optical biosensor utilizing surface plasmon resonance," in *Proc. IEEE Int. Instrum. Meas. Technol. Conf.*, May 2014, pp. 890–895.

[12] X. Li, N. B. Hassan, A. Burton, Z. Ghassemlooy, S. Zvanovec, and R. Perez-Jimenez, "A simplified model for the rolling shutter based camera in optical camera communications," in *Proc. 15th Int. Conf. Telecommun. (ConTEL)*, Jul. 2019, pp. 1–5.

[13] P. Chavez-Burbano, V. Guerra, J. Rabadan, and R. Perez-Jimenez, "Optical camera communication for smart cities," in *Proc. IEEE/CIC Int. Conf. Commun. China (ICCC Workshops)*, Oct. 2017, pp. 1–4.

[14] A. Liu, W. Shi, M. Ouyang, and W. Liu, "Characterization of optical camera communication based on a comprehensive system model," *J. Lightw. Technol.*, vol. 40, no. 18, pp. 6087–6100, Sep. 15, 2022.

[15] J. C. Chau and T. D. C. Little, "Analysis of CMOS active pixel sensors as linear shift-invariant receivers," in *Proc. IEEE Int. Conf. Commun. Workshop (ICCW)*, Jun. 2015, pp. 1398–1403.

[16] A. Liu, W. Shi, W. Liu, and Z. Wang, "A simplified system model for optical camera communication," in *Proc. IEEE/CIC Int. Conf. Commun. China (ICCC)*, Jul. 2021, pp. 911–915.

[17] N. M. Esfahani, A. Gholami, N. S. Kordavani, S. Zvanovec, and Z. Ghassemlooy, "The impact of camera parameters on the performance of V2V optical camera communications," in *Proc. 12th Int. Symp. Commun. Syst., Netw. Digit. Signal Process. (CSNDSP)*, Jul. 2020, pp. 1–4.

[18] J. Leuermann et al., "Coherent silicon photonic interferometric biosensor with an inexpensive laser source for sensitive label-free immunoassays," *Opt. Lett.*, vol. 45, no. 24, pp. 6595–6598, 2020.

[19] J. G. Wangüemert-Pérez et al., "Subwavelength structures for silicon photonics biosensing," *Opt. Laser Technol.*, vol. 109, pp. 437–448, 2019.

[20] P. J. Reyes-Iglesias, I. Molina-Fernández, A. Moscoso-Mártir, and A. Ortega-Moñux, "High-performance monolithically integrated 120° downconverter with relaxed hardware constraints," *Opt. Exp.*, vol. 20, no. 5, p. 5725, 2012.

[21] R. Halir, L. Vivien, X. Le Roux, D.-X. Xu, and P. Cheben, "Direct and sensitive phase readout for integrated waveguide sensors," *IEEE Photon. J.*, vol. 5, no. 4, pp. 1–16, Aug. 2013.

[22] *EMVA Standard 1288–standard for Characterization of Image Sensors and Cameras*, Eur. Mach. Vis. Assoc., Barcelona, Spain, 2016, pp. 18–20.

[23] J. R. Janesick, *Photon Transfer*. Bellingham, WA, USA: SPIE, 2007.

[24] M. Konnik and J. Welsh, "High-level numerical simulations of noise in CCD and CMOS photosensors: Review and tutorial," 2014, *arXiv:1412.4031*.

[25] H. Zhang, C. Li, X. Tu, X. Luo, M. Yu, and P. G.-Q. Lo, "High efficiency silicon nitride grating coupler," *Appl. Phys. A, Solids Surf.*, vol. 115, no. 1, pp. 79–82, Apr. 2014.

[26] V. Vitali, C. Lacava, T. Domínguez Bucio, F. Y. Gardes, and P. Petropoulos, "Highly efficient dual-level grating couplers for silicon nitride photonics," *Sci. Rep.*, vol. 12, no. 1, p. 15436, Sep. 2022.

[27] Photometrics.(2019). *Control of Noise and Background in Scientific Cmos Technology*. Accessed: Jun. 11, 2024. [Online]. Available: https://www.photometrics.com/wp-content/uploads/2019/11/Control-of-Noise-and-Background-in-Scientific-CMOS-Technology.pdf

[28] A. C. Moore, "Quantum efficiency overestimation and deterministic cross talk resulting from interpixel capacitance," *Opt. Eng.*, vol. 45, no. 7, Jul. 2006, Art. no. 076402.

[29] L. Cheng, S. Mao, Z. Li, Y. Han, and H. Fu, "Grating couplers on silicon photonics: Design principles, emerging trends and practical issues," *Micromachines*, vol. 11, no. 7, p. 666, Jul. 2020.

[30] J. Wang, M. M. Sanchez, Y. Yin, R. Herzer, L. Ma, and O. G. Schmidt, "Silicon-based integrated label-free optofluidic biosensors: Latest advances and roadmap," *Adv. Mater. Technol.*, vol. 5, no. 6, Jun. 2020, Art. no. 1901138.

[31] R. J. J. van Gulik, B. M. de Boer, and P. J. Harmsma, "Refractive index sensing using a three-port interferometer and comparison with ring resonators," *IEEE J. Sel. Topics Quantum Electron.*, vol. 23, no. 2, pp. 433–439, Mar. 2017.

[32] B. Lisboa et al., "Nanoporous graphene integrated onto bimodal waveguide biosensors for detection of C-reactive protein," *ACS Appl. Nano Mater.*, vol. 8, no. 3, pp. 1640–1648, Jan. 2025.

[33] B. Bassols-Cornudella et al., "Novel sensing algorithm for linear read-out of bimodal waveguide interferometric biosensors," *J. Lightw. Technol.*, vol. 40, no. 1, pp. 237–244, Jan. 15, 2022.

[34] M. S. Murib, D. Martens, and P. Bienstman, "Label-free real-time optical monitoring of DNA hybridization using SiN Mach–Zehnder interferometer-based integrated biosensing platform," *J. Biomed. Opt.*, vol. 23, no. 12, 2018, Art. no. 127002.